Journal of Solid State Chemistry 186 (2012) 224–230

Contents lists available at SciVerse ScienceDirect

Journal of Solid State Chemistry

journal homepage: www.elsevier.com/locate/jssc

The reaction mechanism of formation of chemically synthesized $Nd_2Fe_{14}B$ hard magnetic nanoparticles

P.K. Deheri, S. Shukla, R.V. Ramanujan *

School of Materials Science and Engineering, Division of Materials Science, Nanyang Technological University, Singapore 639 798, Singapore

ARTICLE INFO

Article history:
Received 5 August 2011
Received in revised form
27 September 2011
Accepted 13 November 2011
Available online 9 December 2011

Keywords:
Magnetic nanoparticles
Chemical synthesis
Reduction–diffusion (R–D) method
Mechanism of formation

ABSTRACT

$Nd_2Fe_{14}B$ based magnetic materials exhibit excellent magnetic properties and are widely used in many engineering applications. However, chemical synthesis of this compound is challenging. In this work, the formation mechanism of chemically synthesized $Nd_2Fe_{14}B$ magnetic nanoparticles was studied. Nd, Fe and B precursors were converted to Nd–Fe–B oxide by the sol–gel method, reduction of these oxides by CaH_2 resulted in $Nd_2Fe_{14}B$ nanoparticles. $Nd_2Fe_{14}B$ phase formation resulted from two competing reactions: (a) $Nd_2Fe_{14}B$ phase formation by direct combination of NdH_2, Fe and B, (b) Nd_2Fe_{17} phase formation from NdH_2 and Fe, followed by $Nd_2Fe_{14}B$ phase formation by the reaction of Nd_2Fe_{17} and B. Addition of boron to Nd–Fe–B oxide during reduction resulted in improved magnetic properties. The activation energy for $Nd_2Fe_{14}B$ phase formation was found to be 365 kJ mol^{-1}. The optimum heat treatment temperature and time for $Nd_2Fe_{14}B$ phase formation were found to be 800 °C and 90 min, respectively.

1. Introduction

Rare earth based Nd–Fe–B permanent magnetic materials have an enormous range of technological applications due to their excellent combination of high coercivity and energy product $(BH)_{max}$. These permanent magnets in bulk form are used in electric motors, generators, magnetic separators, magnetic levitation systems and loud speakers. $Nd_2Fe_{14}B$ based powders are used in preparation of sintered magnets and bonded magnets [1]. $Nd_2Fe_{14}B$ magnetic nanostructured materials have found applications in sensors, transducers, magnetic fluids and in magnetic elastomers [2–4]. At the industrial level, these intermetallic compounds are synthesized by physical methods such as melt spinning and the ball milling routes [5–7]. However, physical methods impose a number of limitations on the alloy composition, particle size control and the form of the final magnet. Hence, there has been an intense effort to process these magnetic materials by chemical synthesis techniques [8–10]. However, due to the large difference in the reduction potential, co-reduction of transition metal and rare earth elements is challenging [11]. Solution based synthesis combined with high temperature solid state reduction has been shown to be a successful method to prepare Sm–Co hard magnetic nanoparticles [12]. One potential chemical route to prepare Nd–Fe–B magnetic nanoparticles is the use of the sol–gel method to produce Nd–Fe–B mixed oxide followed by reduction–diffusion (R–D) to produce $Nd_2Fe_{14}B$ based alloys. Reduction–diffusion (R–D) involves reduction of Nd–Fe–B oxide by calcium or calcium hydride to produce $Nd_2Fe_{14}B$ and CaO [13–18]. The CaO can be removed by washing with water to obtain the desired $Nd_2Fe_{14}B$ nanoparticles.

Besides technological applications, the magnetic properties of nanoparticles are also of fundamental scientific interest due to single domain particle magnetism and superparamagnetism [19]. Moreover, extrinsic magnetic properties such as coercivity and remanant magnetization are size and shape dependant, hence it is essential to understand the kinetics and mechanism of the formation of crystallization products. This will enable us to control shape and size of particles at the nanoscale. Hence, determination of the kinetics and the mechanism of formation of $Nd_2Fe_{14}B$ nanoparticles is of considerable research interest. Synthesis of $Nd_2Fe_{14}B$ by chemical routes offers the possibility of size and shape control by control of the nucleation and growth of particles [20]. The nanoparticle size can be controlled by adjusting reaction parameters, such as time, temperature and concentration of reagents [21]. For example, during reduction of metal salts by sodium borohydride, rapid injection of the reducing agent results in a high nucleation rate. Subsequently, the reducing agent can be added slowly to control growth [22]. In an alternative process, reagents are mixed at low temperature and slowly heated at a controlled rate to induce nucleation. The particle size subsequently increases by Ostwald ripening [23]. Growth can be

* Corresponding author. Fax: +65 6790 9081.
E-mail addresses: DEHE0001@e.ntu.edu.sg (P.K. Deheri), shukla@pmail.ntu.edu.sg (S. Shukla), Ramanujan@ntu.edu.sg (R.V. Ramanujan).

0022-4596/$ - see front matter © 2011 Elsevier Inc. All rights reserved.
doi:10.1016/j.jssc.2011.11.022

minimized by decreasing the reaction temperature or minimizing the availability of the relevant reactant [21,22]. In the reduction–diffusion process, growth can be controlled by controlling the reaction temperature and time [24]. The anisotropic growth of particles determines the particle shape and can be either diffusion controlled or reaction controlled [25].

The reduction–diffusion (R–D) process has been previously reported as a promising technique to produce $Nd_2Fe_{14}B$ based magnetic nanoparticles [15,26]. In such solid state reactions, determination of the kinetics, rate controlling steps and kinetic parameters such as activation energy provide valuable insights into the reaction mechanism [27,28]. Sidhu and Verma [24] have studied the kinetics of formation of $Nd_2Fe_{14}B$ by calciothermic reaction, however, the mechanism and kinetics were not clearly identified. Hence, we studied the kinetics, thermodynamic and mechanism of synthesis of $Nd_2Fe_{14}B$ by first preparing Nd–Fe–B oxide by the sol–gel, followed by reduction–diffusion (R–D) process to produce $Nd_2Fe_{14}B$ nanoparticles. Differential scanning calorimetry (DSC), X-ray diffraction (XRD) and transmission electron microscopy (TEM) techniques were used in this study. The reduction–diffusion (R–D) was a three step process: reduction of Fe_2O_3 to Fe and B_2O_3 to B at 300 °C, followed by reduction of Nd_2O_3 and $NdFeO_3$ to NdH_2 and Fe at 620 °C. In the final step, $Nd_2Fe_{14}B$ phase formation occurred. This was the result of two concurrent competing reactions. One reaction involved direct combination of NdH_2, Fe and B to form $Nd_2Fe_{14}B$ phase, while in the other reaction the formation of Nd_2Fe_{17} from NdH_2 and Fe occurred, followed by $Nd_2Fe_{14}B$ phase formation by reaction of Nd_2Fe_{17} with B. Addition of amorphous boron to Nd–Fe–B oxide during reduction resulted in increased $Nd_2Fe_{14}B$ mass percentage and improved magnetic properties. The activation energy for $Nd_2Fe_{14}B$ phase formation (E_a) was found to be

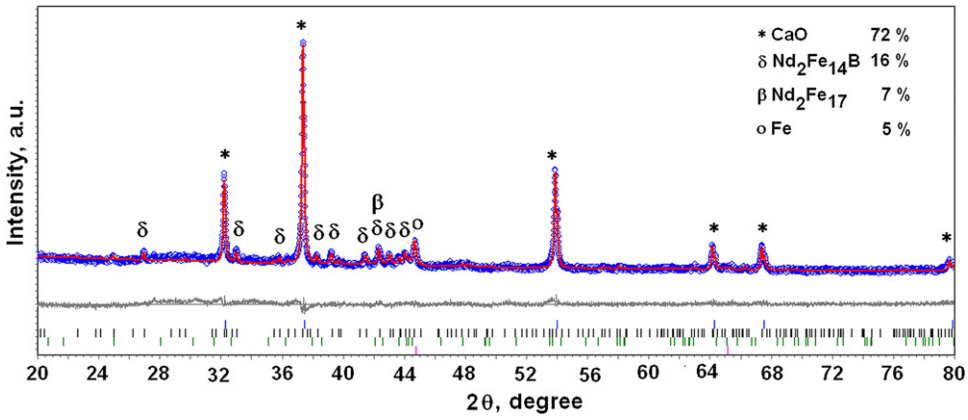

Fig. 1. Rietveld refinement of Nd–Fe–B alloy nanoparticles synthesized by sol–gel followed by reduction–diffusion. The phases present are $Nd_2Fe_{14}B$, α-Fe and CaO. Nd_2Fe_{17} phase was also observed due to boron loss during reduction.

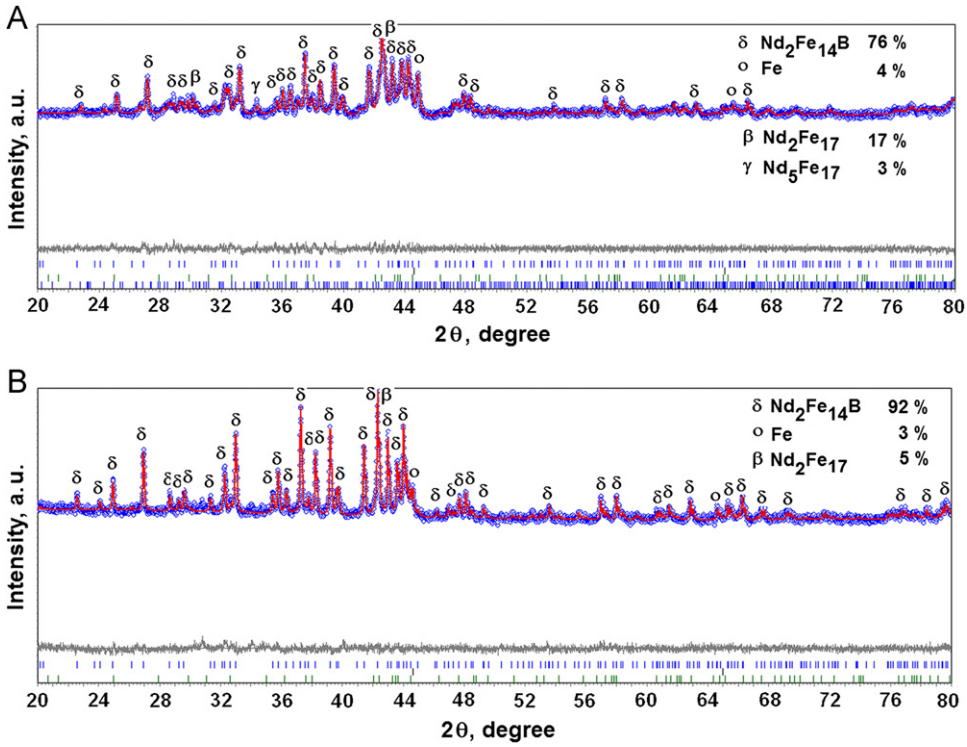

Fig. 2. Rietveld refinement of Nd–Fe–B synthesized by sol–gel followed by reduction–diffusion: (A) without boron (800 °C, 90 min) and (B) with 0.2 wt% of amorphous boron (800 °C, 90 min). Weight percent of Nd_2Fe_{17} phase is decreased with boron addition.

365 kJ mol^{-1}. The activation energies corresponding to α-Fe formation and NdH_2 formation were 96 kJ mol^{-1} and 409 kJ mol^{-1}, respectively. The optimum heat treatment temperature and time for $Nd_2Fe_{14}B$ phase formation were found to be 800 °C and 90 min, respectively.

2. Experimental

Neodymium chloride hexahydrate ($NdCl_3 \cdot 6H_2O$, 99.9%), iron chloride hexahydrate ($FeCl_3 \cdot 6H_2O$, 97–102%), boric acid (H_3BO_3, 99.8%), citric acid (99.5%) and ethylene glycol (99%) from Alfa Aesar, CaH_2 (90–95%, Sigma) were used for synthesis. The synthesis of Nd–Fe–B oxide was carried out by a Pechini type sol–gel process [29]. In a typical experiment, nominal composition of $Nd_{15}Fe_{77.5}B_{7.5}$ was selected, which had been previously shown to result in the maximum mass percentage of $Nd_2Fe_{14}B$ phase and good magnetic properties [26]. Stoichiometric quantity of neodymium chloride hexahydrate, iron chloride hexahydrate and boric acid were dissolved in deionized water. Then citric acid and ethylene glycol in 2:1 molar ratio to metal salts were added to prepare a thermally stable sol. The mixed solution was heated at 90 °C overnight resulting a viscous gel, the gel was then dried at 200 °C. The dried gel was then heated at 400 °C for 2 h, followed by 800 °C for 2 h. to prepare Nd–Fe–B oxide powder. These oxides were analyzed by X-ray diffraction and used in the subsequent reduction–diffusion (R–D) process to form $Nd_2Fe_{14}B$ powder particles. The $Nd_2Fe_{14}B$ powder morphologies were examined by transmission electron microscope (JEOL-TEM 2010, 200 kV).

2.1. Kinetics

The mixture of Nd–Fe–B oxide and CaH_2 were heat treated in a vacuum furnace (10^{-5} Pa) at a heating rate of 15 K/min and the reaction products were analyzed by XRD techniques. The phases formed were identified by a Bruker AXS X-ray diffractometer (Cu$K\alpha$ radiation, $\lambda = 0.154$ nm). The XRD data were collected in the 2θ range of 20–120° with a 0.01 step size. Rietveld refinement was carried out using the software program TOPAS 4. Tetragonal $Nd_2Fe_{14}B$ (space group $P42/mnm$), $Nd_2Fe_{14}BH_{4.7}$ (space group $P42/mnm$) and α-Fe (space group $Im\text{-}3m$) were taken as the starting model. The mass percentage obtained by the Rietveld refinement was used for kinetic study. To minimize the mass percentage of Nd_2Fe_{17} phase in the final product, 0.2 wt% of amorphous boron was added to Nd–Fe–B oxide. Isothermal DSC of mixtures of Nd–Fe–B oxide, amorphous boron and CaH_2 powders were carried out at temperatures of 265 °C, 616 °C and 650 °C.

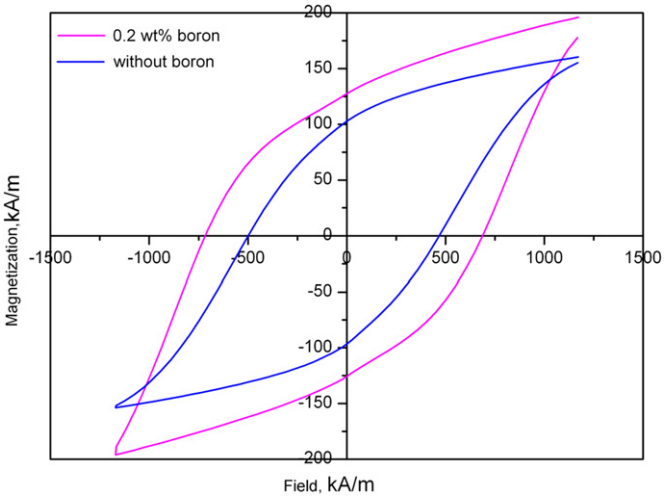

Fig. 3. Room temperature VSM properties of Nd–Fe–B synthesized by sol–gel followed by reduction–diffusion method (as synthesized, with and without boron addition). Magnetic properties increased with 0.2 wt% of amorphous boron addition.

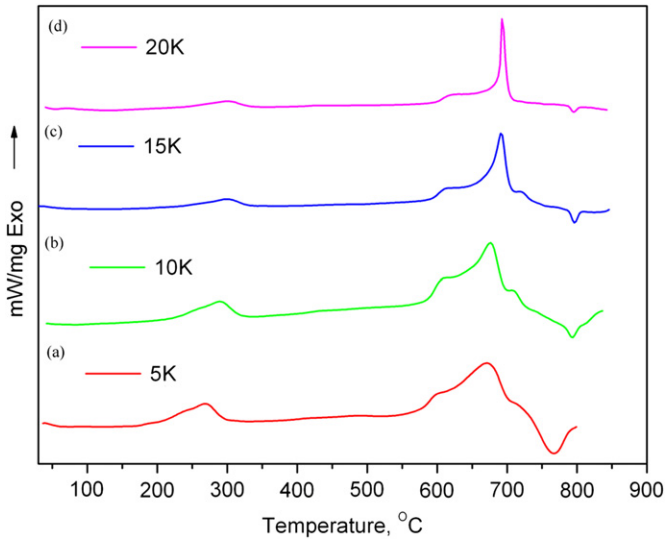

Fig. 5. Isochronal DSC of Nd–Fe–B oxide+0.2 wt% B+1.4 wt% of CaH_2 at heating rates of (a) 5 K min^{-1}, (b) 10 K min^{-1}, (c) 15 K min^{-1}, and (d) 20 K min^{-1}.

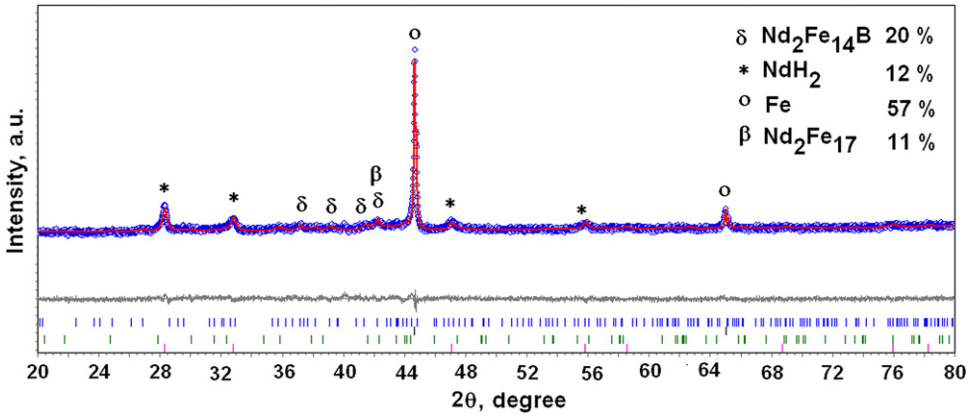

Fig. 4. Rietveld refinement of Nd–Fe–B synthesized by sol–gel followed by reduction–diffusion at 650 °C (42 °C below the $Nd_2Fe_{14}B$ phase transformation peak temperature of DSC). Both $Nd_2Fe_{14}B$ and Nd_2Fe_{17} phases are formed at this temperature.

2.2. Activation energy determination

To determine the activation energy of reduction of Nd–Fe–B oxide to form $Nd_2Fe_{14}B$ and α-Fe phases, isochronal DSC measurements of mixtures of Nd–Fe–B oxide, 0.2 wt% amorphous boron and 1.4 wt% CaH_2 were carried out in argon using a Netzsch DSC-404 at heating rates of 5 K, 10 K, 15 K and 20 K per minute.

3. Results and discussion

3.1. Synthesis of $Nd_2Fe_{14}B$ nanoparticles

Solution based synthesis followed by reduction–diffusion (R–D) was found to be a successful method to produce rare-earth magnetic nanoparticles [12,18,26]. The synthesis consists of two

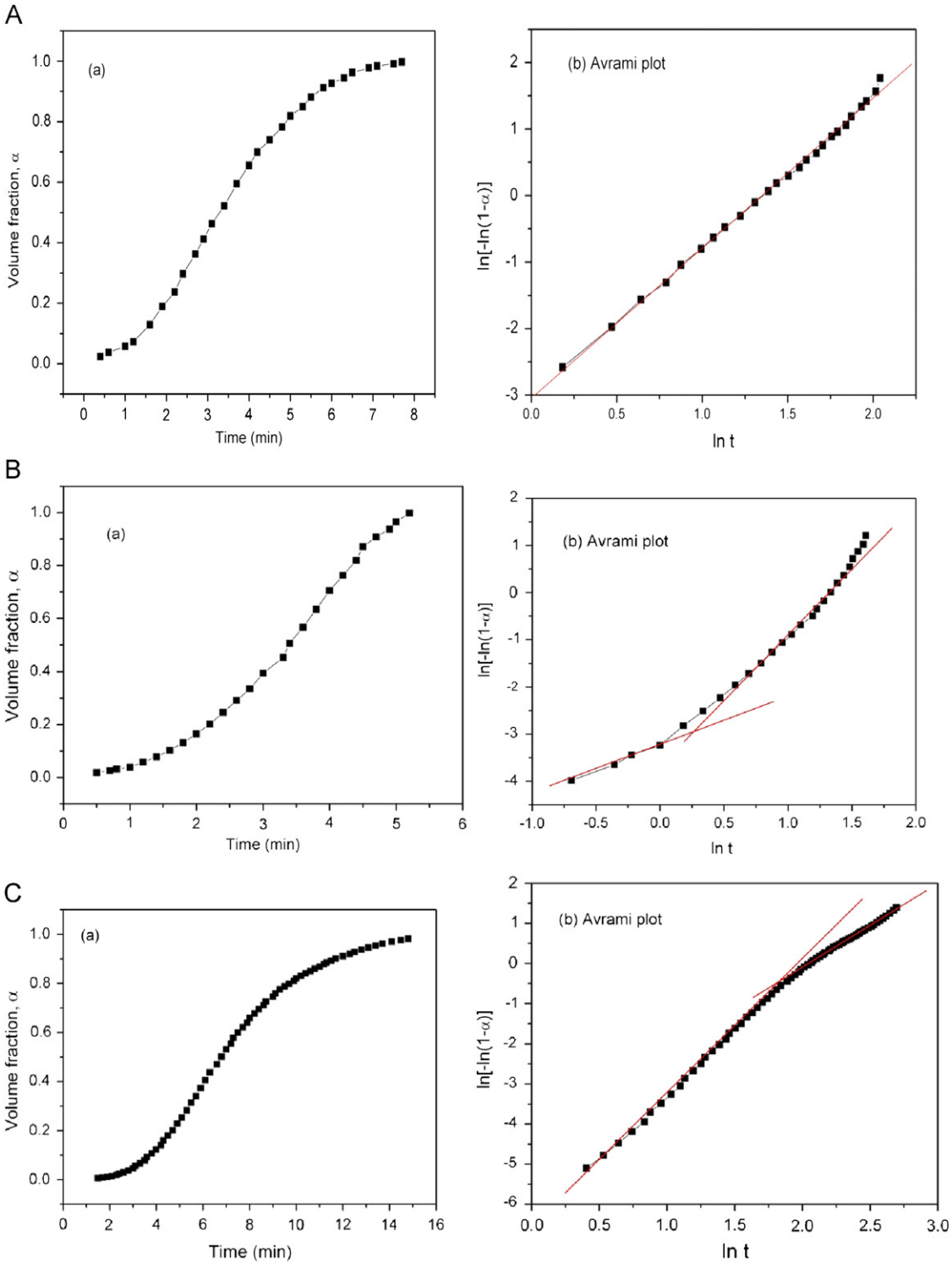

Fig. 6. (A) JMA plot corresponding to Fe_2O_3 and B_2O_3 reduction, (B) JMA plot corresponding to Nd_2O_3 and $NdFeO_3$ reduction and (C) JMA plot corresponding to $Nd_2Fe_{14}B$ formation.

steps: Nd–Fe–B oxide preparation by sol–gel method followed by reduction–diffusion (R–D) by CaH_2 [26]. The Nd–Fe–B gel was a Nd–Fe–B–citrate complex cross linked by ethylene glycol [26]. The Nd–Fe–B oxide which was obtained by heating this Nd–Fe–B gel, was found to be a mixture of Nd_2O_3, $NdFeO_3$, Fe_2O_3 and B_2O_3 oxides [26]. Annealing of the mixture of Nd–Fe–B oxide and CaH_2 in the mass ratio of 1:1.4, respectively, resulted in the formation of a mixture of $Nd_2Fe_{14}B$, Nd_2Fe_{17}, α-Fe and CaO phases (Fig. 1). The CaO phase was removed by washing with dilute acetic acid and deionized water to isolate the magnetic nanoparticles. Fig. 2 shows the Rietveld refined data of CaO removed samples. The final products also contained ~16 wt% of Nd_2Fe_{17} phase (Fig. 2A). The addition of 0.2 wt% of amorphous boron to the mixture of Nd–Fe–B oxide and CaH_2, reduced the weight percent of the Nd_2Fe_{17} phase to ~5 wt% (Fig. 2B). The magnetic properties were improved by amorphous boron addition (Fig. 3); coercivity increased from ~500 to ~700 kA m^{-1} and magnetization increased from 160 to 196 kA m^{-1}. The maximum weight percent of the $Nd_2Fe_{14}B$ phase was found to be ~92 wt% (Fig. 2B), for 90 min reduction at 800 °C. This mass percentage was later used in the mass fraction calculation for kinetic conversion studies.

3.2. Formation mechanism of $Nd_2Fe_{14}B$

Recently, the reduction–diffusion (R–D) mechanism of $Nd_2Fe_{14}B$ formation from Nd–Fe–B oxide was studied, the steps are [26]:

$$\text{Step 1—at 300 °C: } Fe_2O_3+3CaH_2\rightarrow 2Fe+3CaO+3H_2\uparrow \quad (1)$$

$$B_2O_3+3CaH_2\rightarrow 2B+3CaO+3H_2\uparrow \quad (2)$$

$$\text{Step 2—at 620 °C: } Nd_2O_3+3CaH_2\rightarrow 2NdH_2+3CaO+H_2\uparrow \quad (3)$$

$$NdFeO_3+3CaH_2\rightarrow NdH_2+Fe+3CaO+2H_2\uparrow \quad (4)$$

$$\text{Step 3—at 692 °C: } 2NdH_2+14Fe+B\rightarrow Nd_2Fe_{14}B+2H_2\uparrow \quad (5)$$

Reitveld refinement analysis of the reduction–diffusion (R–D) product formed at 650 °C, showed that both $Nd_2Fe_{14}B$ and Nd_2Fe_{17} phases were formed (Fig. 4). The formation of $Nd_2Fe_{14}B$ phase was by either (a) direct combination of NdH_2, Fe and B (reaction (5)), or (b) by Nd_2Fe_{17} phase formation which includes additional reactions (reactions (6) and (7)).

$$\text{Step 3—at 692 °C: } 2NdH_2+17Fe\rightarrow Nd_2Fe_{17}+2H_2\uparrow \quad (6)$$

$$Nd_2Fe_{17}+B\rightarrow Nd_2Fe_{14}B+3Fe \quad (7)$$

Isothermal DSC was also carried out at 650 °C to study the $Nd_2Fe_{14}B$ phase formation kinetics. $Nd_2Fe_{14}B$ phase formation by two competing reactions was further validated by the exothermic peak shoulder (Fig. 5) [30]. A broad shoulder was observed for ischronal DSC study at a heating rate of 5 K min^{-1} while a single peak was observed for 20 K min^{-1} rate. This observation suggested that the order of reactions 5, 6 and 7 is greater than one; when the reaction order is equal to one only a single peak is observed [30]. This further showed that the values of activation energy and the pre-exponential factors of both the reaction paths (reactions (5)–(7)) were different [30], and the dominance of reaction paths were dependant on heating rate.

3.3. Kinetics

3.3.1. Differential scanning calorimetry

Isothermal DSC measurements were carried out to investigate the kinetics of the reduction–diffusion (R–D) process of $Nd_2Fe_{14}B$ formation. To study nucleation and growth, isothermal DSC measurements were performed at temperatures lower than the peak temperature of 300, 620 and 692 °C. A theoretical basis for the interpretation of isothermal DSC data was provided by Avrami [31,32] and describes the evolution of the volume fraction crystallized (α) as a function of time t. The fraction of phase formed $\alpha(t)$, can be expressed as

$$\alpha(t)=1-e^{-(kt)^n} \quad (8)$$

where k is the rate constant and reflects the rate of nucleation and growth. The variable n is the Avrami exponent and depends on the type of nucleation and growth process. The fraction of phase formed was determined by calculating the fractional area of the isothermal peak. The value of k and n can be calculated from Eq. (8), which can be rearranged as

$$\ln[-\ln(1-\alpha)]=n\ln k+n\ln t \quad (9)$$

A plot of $\ln[-\ln(1-\alpha)]$ vs. $\ln t$ is called the Johnson–Mehl–Avrami (JMA) plot [31,32], the JMA plot for the reduction process and $Nd_2Fe_{14}B$ phase formation is shown in Fig. 6. The Avrami exponent n and kinetic constant k were calculated from the slope and intercept of the plot.

The Avrami exponent for the reductions of Fe_2O_3 and B_2O_3 was 1.96 (for reactions (1) and (2)). However, the JMA plots for reductions of Nd_2O_3 and $NdFeO_3$ (reactions (3) and (4)) and for $Nd_2Fe_{14}B$ phase formation (reactions (5)–(7)) were not straight line but could be approximated by two linear steps, due to two steps with different nucleation and growth kinetics. The first step in the reactions 3 and 4, the Avrami exponent was 1.1 followed by 2.6 in the second step. The Avrami exponents for $Nd_2Fe_{14}B$ phase formation were 3.2 and 2.1 for first and second steps, respectively. The value of Avrami exponent of 3.0 represents isotropic crystal growth [33], lower values represent lower dimensional growth. TEM analysis showed inhomogeneous morphology (Fig. 7) and nano-rod shape (Fig. 8), this anisotropic factor could be responsible for the Avrami exponent value being lower than 3.

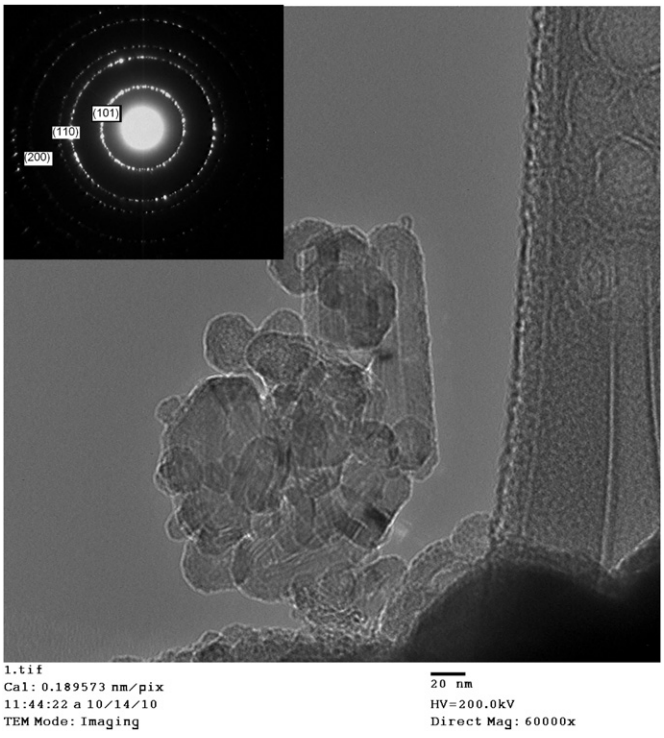

Fig. 7. Bright field transmission electron micrograph of $Nd_2Fe_{14}B$ synthesized by sol–gel method, the SADP is indexed to $Nd_2Fe_{14}B$.

3.3.2. X-ray diffraction

For this alloy composition the pseudo-binary phase diagram does not show the Nd_2Fe_{17} phase [34]. However, the metastable Nd_2Fe_{17} phase formed (reaction (6)), could only be removed (reaction (7)) very slowly (Fig. 9). The mass percentage of Nd_2Fe_{17} phase fluctuated with reduction time for reduction temperatures of 692 °C and 750 °C (Fig. 9). This type of fluctuation reaction may be due to the stochastic nature of the processes of reduction and diffusion and limits the applicability of Avrami exponent calculations in this temperature range. This mass fluctuation is consistent with the competing nature of the formation reactions of $Nd_2Fe_{14}B$ by direct combination of NdH_2, Fe, B (reaction (5)) and via Nd_2Fe_{17} intermediate formation (reactions (6) and (7)). There was no reaction fluctuation at 800 °C (Fig. 10). The reaction mixture annealed at 800 °C for 90 min produced $Nd_2Fe_{14}B$ nanoparticles and a smaller mass percentage of the Nd_2Fe_{17} phase (Figs. 10A and 2B). The Avrami exponent for $Nd_2Fe_{14}B$ phase formation at 800 °C was calculated to be 1.8 (Fig. 10B).

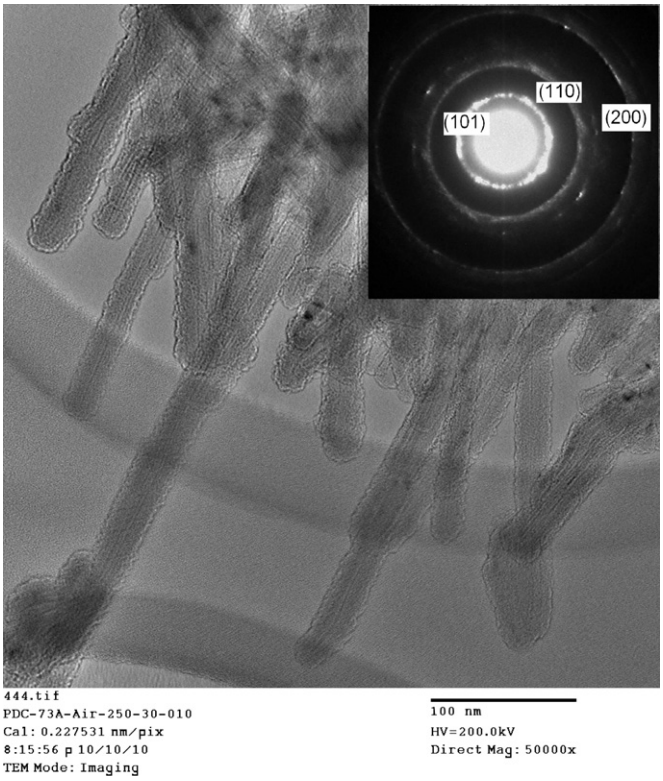

Fig. 8. Bright field transmission electron micrograph of $Nd_2Fe_{14}B$ synthesized by sol–gel method, the SADP is indexed to $Nd_2Fe_{14}B$. Inhomogeneous (Fig. 7) and nanorod morphology (Fig. 8) were observed for the identical reduction–diffusion (R–D) conditions.

3.4. Activation energy of $Nd_2Fe_{14}B$ phase formation by reduction–diffusion (R–D) process

The activation energy is usually evaluated from isochronal DSC thermograms obtained at various heating rates [35]. The activation energy of phase formation can be characterized by activation energies of nucleation and growth. The compounded activation energy of both nucleation and growth was calculated using the Kissinger model [35]. The peak temperature T_p and heating rate b are related to the activation energy (E_a) by

$$\ln \frac{b}{T_p^2} = -\frac{E_a}{RT_p} + C \tag{10}$$

The activation energy (E_a) was determined from the slope of the $\ln(b/T_p^2)$ vs. $1000/T_p$ curve. The typical DSC of the reduction–diffusion (R–D) process for different heating rates is shown in Fig. 5. The first two peaks correspond to reduction reactions, the peak near 692 °C corresponds to $Nd_2Fe_{14}B$ phase formation. The endothermic peak near 800 °C corresponds to the melting point of calcium.

The plot of $\ln(b/T_p^2)$ vs. $1000/T_p$ for $Nd_2Fe_{14}B$ phase formation is shown in Fig. 11. Since, $Nd_2Fe_{14}B$ phase formation was a multistep reaction (reactions (5)–(7)), the calculated activation energy corresponded to the overall reaction, E_a was calculated to be 365 kJ mol^{-1}. This activation energy was eight fold larger than the activation energy calculated for $TbFe_2$ phase formation by reduction–diffusion (R–D) [36]. The activation energy corresponding to the first two peaks were 96 kJ mol^{-1} (Fe and B formation) and 409 kJ mol^{-1} (NdH_2 formation), respectively. The activation energy of NdH_2 formation from Nd_2O_3 and $NdFeO_3$ was higher than the activation energy of Fe and B formation from Fe_2O_3 and B_2O_3, respectively, and that of $Nd_2Fe_{14}B$ phase formation.

4. Conclusions

Isochronal and isothermal DSC, XRD and TEM analyses were used to study the $Nd_2Fe_{14}B$ phase formation from Nd–Fe–B oxide powders produced by the sol–gel technique.

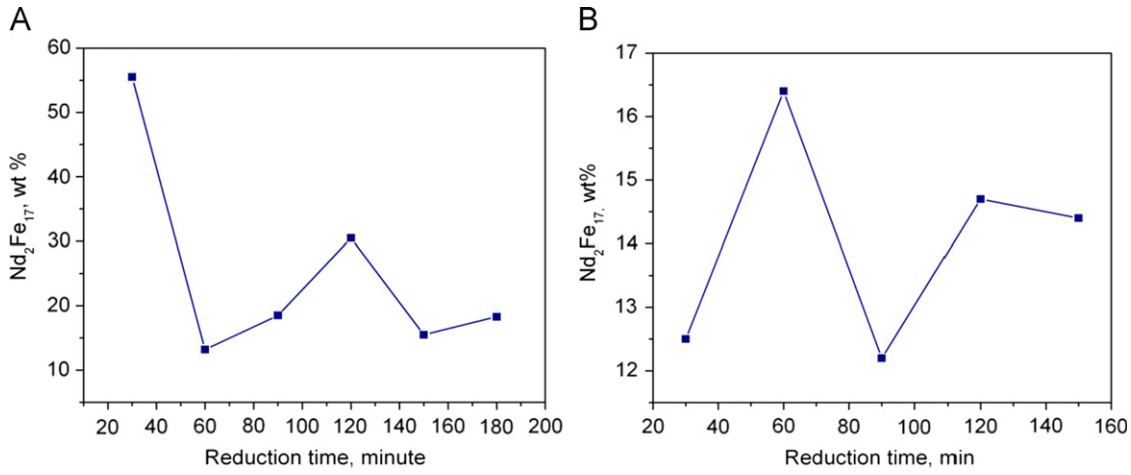

Fig. 9. Mass percentage of Nd_2Fe_{17} with reduction time annealed at (A) 692 °C and (B) 750 °C. In these temperature ranges the mass percentage of Nd_2Fe_{17} formation fluctuates with reduction time.

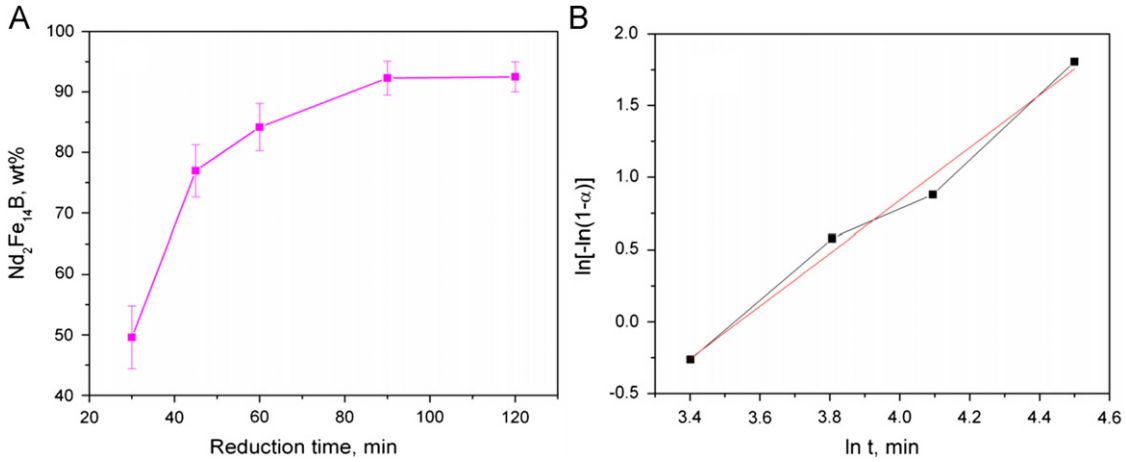

Fig. 10. (A) Mass percentage of $Nd_2Fe_{14}B$ and Nd_2Fe_{17} phase formation at 800 °C and (B) Avrami plot corresponding to $Nd_2Fe_{14}B$ phase formation at 800 °C.

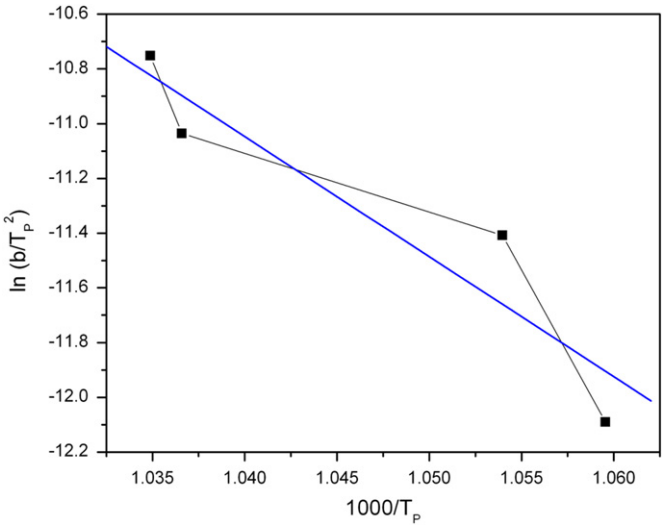

Fig. 11. $\ln(b/T_p^2)$ vs. $1000/T_p$ plot for $Nd_2Fe_{14}B$ phase formation.

1. Reduction–diffusion (R–D) was a three-step process: (a) reduction of Fe_2O_3 and B_2O_3 to form Fe and B at 300 °C, (b) reduction of Nd_2O_3 and $NdFeO_3$ to form NdH_2 and Fe at 620 °C and (c) $Nd_2Fe_{14}B$ phase formation at 692 °C.
2. $Nd_2Fe_{14}B$ phase formation was combination of two parallel competing reactions: (a) by direct combination of NdH_2, Fe and B and (b) formation of Nd_2Fe_{17} from NdH_2 and Fe, followed by $Nd_2Fe_{14}B$ phase formation by reaction of Nd_2Fe_{17} with B.
3. Addition of amorphous boron to Nd–Fe–B oxide during reduction resulted in increased $Nd_2Fe_{14}B$ mass percentage at the cost of Nd_2Fe_{17} phase and improved magnetic properties; the coercivity increased from ~500 to ~700 kA $m^{-1}$and magnetization increased from 160 to 196 kA m^{-1}.
4. The activation energy E_a was found to be 365 kJ mol^{-1} for $Nd_2Fe_{14}B$ phase formation.
5. The activation energy corresponding to α-Fe formation and NdH_2 formation was at 96 kJ mol^{-1} and 409 kJ mol^{-1}, respectively.
6. The heat treatment temperature and time for maximum $Nd_2Fe_{14}B$ phase formation were found to be 800 °C and 90 min, respectively.

Acknowledgment

The authors are grateful to the SERC, Singapore for financial support for this work through ASTAR Grant no: 062 101 0032.

References

[1] D. Brown, B.M. Ma, Z. Chen, J. Magn. Magn. Mater. 248 (2002) 432.
[2] R. Setnescu, T. Setnescu, S. Jipa, W. Kappel, M. Dumitru, M.M. Codescu, N. Stancu, T. Zaharescu, J. Optoelectron. Adv. Mater. 8 (2006) 533.
[3] F. Amirouche, Y. Zhou, T. Johnson, Microsyst. Technol. 15 (2009) 647.
[4] Z. Chen, D. Miller, J. Herchenroeder, J. Appl. Phys. 107 (2010) 09A730.
[5] M. Sagawa, S. Fujimura, N. Togawa, H. Yamamoto, Y. Matsuura, J. Appl. Phys. 55 (1984) 2083.
[6] J.J. Croat, J.F. Herbst, R.W. Lee, F.E. Pinkerton, J. Appl. Phys. 55 (1984) 2078.
[7] N.C. Koon, B.N. Das, J. Appl. Phys. 55 (1984) 2063.
[8] Y. Haik, J. Chatterjee, C.Jen Chen, J. Nanopart. Res. 7 (2005) 675.
[9] C.W. Km, Y.H. Km, H.G. Cha, Y.S. Kang, Phys. Scr. T129 (2007) 321.
[10] H.G. Cha, Y.H. Kim, C.W. Kim, Y.S. Kang, IEEE Nanotechnology Materials and Devices Conference, NMDC, Gyeongju, 2006, pp. 656–657.
[11] C.N. Chinnasamy, J.Y. Huang, L.H. Lewis, B. Latha, C. Vittoria, V.G. Harris, Appl. Phys. Lett. 93 (2008) 032505.
[12] B.Y. Hou, Z. Xu, S. Peng, C. Rong, J.P. Liu, S. Sun, Adv. Mater. 19 (2007) 3349.
[13] Y. Okajima, Y. Tsugita, T. Tkechi, S. Okada, U.S. Patent, (1987) 4681,623.
[14] K. Ohmori, K. Shionoya, J. Appl. Phys. 69 (1991) 5504.
[15] R.K. Sidhu, J. Alloys Compd. 346 (2002) 250.
[16] T.S. Jang, D.H. Lee, J.H. Yu, J.C. Choi, S.W. Seo, H.Y. Lee, Rare Met. 25 (2006) 223.
[17] X.L. Dong, B.K. Kim, C.J. Choi, K.S. Park, Z.D. Zhang, J. Mater. Res. 16 (2001) 1083.
[18] S.D. Bhame, V. Swaminathan, P.K. Deheri, R.V. Ramanujan, Adv. Sci. Lett. 3 (2010) 174.
[19] C. Petit, A. Taleb, M.P. Pileni, J. Phys. Chem. B 103 (1999) 1805.
[20] T. Hyeon, Chem. Commun. 9 (2003) 927.
[21] C.B. Murray, S. Sun, W. Gaschler, H. Doyle, T.A. Betley, C.R. Kagan, IBM J. Res. Dev. 45 (2001) 47.
[22] V.F. Puntes, K.M. Krishnan, A.P. Alivisatos, Science 291 (2001) 2115.
[23] B.L. Cushing, V.L. Kolesnichenko, C.J. O'Connor, Chem. Rev. 104 (2004) 3893.
[24] R.K. Sidhu, A. Verma, Processing and Fabrication of Advanced Materials VI, 1998.
[25] T. Sugimoto, Monodispersed particles, Elsevier Science, Netherland, 2001.
[26] P.K. Deheri, V. Swaminathan, S.D. Bhame, Z. Liu, R.V. Ramanujan, Chem. Mater. 22 (2010) 6509.
[27] G.K. Soon, T. Hyeon, Acc. Chem. Res. 41 (2008) 1696.
[28] C. Ghoroi, A.K. Suresh, AlChE J. 53 (2007) 502–513.
[29] M.P. Pechini, U.S. Patent (1967) 3330697.
[30] T. Ozawa, J. Therm. Anal. 9 (1976) 217.
[31] M. Avrami, J. Chem. Phys. 7 (1939) 1103.
[32] M. Avrami, J. Chem. Phys. 8 (1940) 212.
[33] V.S. Raja, Kishore, S. Ranganathan, J. Mater. Sci. 25 (1990) 4667.
[34] W.C. Chang, T.S. Chin, K.S. Liu, J. Magn. Magn. Mater. 80 (1989) 352.
[35] H.E. Kissinger, Anal. Chem. 29 (1957) 1702.
[36] G. Guo, G. Wang, Z. Sui, J. Mater. Sci. Technol. 20 (2004) 68–70.